Microchimica Acta (2020) 187:332
https://doi.org/10.1007/s00604-020-04302-x

ORIGINAL PAPER

# A cardiac troponin I photoelectrochemical immunosensor: nitrogen-doped carbon quantum dots–bismuth oxyiodide–flower-like $SnO_2$

Dawei Fan[1,2] · Xin Liu[1,2] · Xinrong Shao[1,2] · Yong Zhang[1,2] · Nuo Zhang[1,2] · Xueying Wang[1,2] · Qin Wei[1,2] · Huangxian Ju[1,2,3]

Received: 2 January 2020 / Accepted: 27 April 2020


## Abstract

A novel photoelectrochemical (PEC) immunosensor for the determination of cardiac troponin I (cTnI) was constructed. The flower-like stannic oxide ($SnO_2$) with large specific surface area was prepared by hydrothermal synthesis. Nitrogen-doped carbon quantum dots (NCQDs) with excellent surface property were used as a sensitizer for $SnO_2$. Bismuth oxyiodide (BiOI) is a narrow band gap (1.83 eV) nanomaterial, which was firstly modified on NCQDs-sensitized $SnO_2$ through in situ growth method. After NCQDs with small size and BiOI nanoparticles are successively combined with $SnO_2$, the $SnO_2$/NCQDs/BiOI microflower was obtained, which possessed good photochemical properties. Using visible light as excitation source and ascorbic acid (AA) as electron donor, the ultrasensitive and quantitative determination of cTnI was realized by detecting the changes of photocurrent under different concentrations of cTnI. The PEC immunosensor showed a large-scaled response (0.001–100 ng $mL^{-1}$) and a low detection limit (0.3 pg $mL^{-1}$) under optimised experimental conditions. The sensor has potential clinical value in the prediction and diagnosis of cardiovascular diseases in elderly patients with diabetes.

**Keywords** Photoelectrochemical immunosensor · Stannic oxide · Nitrogen-doped carbon quantum dots · Bismuth oxyiodide · Cardiac troponin I

## Introduction

The term photoelectrochemical (PEC) reflects the electrochemical behavior of semiconductor under light illumination [1, 2]. PEC analysis is developed based on the photocurrent or photovoltage signal changes resulting from the physical and chemical interactions between the analyte and photoactive substance [3–5]. Light is as excitation signal, and electrical signal is as detection signal. This method has the advantages of high sensitivity and simple equipment and has been widely used in many fields [6–8]. Therefore, the successful construction of the PEC immunosensor has high potential application value in disease prevention and diagnosis [9–12].

The selection of semiconductor materials with excellent photocatalytic and photoconversion characteristics is crucial for the construction of PEC immunosensors [13–17]. In our work, $SnO_2$ microflowers, which possess porous structure, were successfully prepared by hydrothermal method [18], which provides good stability and large specific surface area of the $SnO_2$ microflower. As a wide band gap (3.60 eV) semiconductor material, the photochemical activity of $SnO_2$ was

**Electronic supplementary material** The online version of this article (https://doi.org/10.1007/s00604-020-04302-x) contains supplementary material, which is available to authorized users.

✉ Dawei Fan
jndxfandawei@126.com

✉ Huangxian Ju
hxju@nju.edu.cn

[1] Collaborative Innovation Center for Green Chemical Manufacturing and Accurate Detection, School of Chemistry and Chemical Engineering, University of Jinan, Jinan 250022, People's Republic of China

[2] Key Laboratory of Interfacial Reaction & Sensing Analysis in Universities of Shandong, School of Chemistry and Chemical Engineering, University of Jinan, Jinan 250022, People's Republic of China

[3] Key Laboratory of Analytical Chemistry for Life Science, School of Chemistry and Chemical Engineering, Nanjing University, Nanjing 210023, People's Republic of China

Published online: 16 May 2020

relatively weaker [19, 20]. However, the large specific surface area of $SnO_2$ had one advantage that could combine more nanoparticles with excellent photochemical properties [21–23]. Based on it, nitrogen-doped carbon quantum dots (NCQDs) with excellent surface properties and fluorescence characteristics were modified on $SnO_2$ to obtain $SnO_2$/NCQDs composites. The addition of NCQDs improved the photochemical activity of $SnO_2$. Recently, NCQDs, which possess strong anti-interference ability, good water solubility, small size, and good dispersion and compatibility, have been widely used in catalysis, imaging, sensing, and other fields [24–27]. Therefore, NCQDs could be used not only as a sensitizer for $SnO_2$ but also as a carboxyl linker in the construction of PEC immunosensor.

Bismuth oxyiodide (BiOI), a narrow band gap (1.83 eV) nanomaterial, possesses high photocatalytic activity under visible light irradiation [28, 29]. In addition, as a cost-effective and promising visible photocatalyst, BiOI has been widely used in many studies. BiOI is conductive to the separation of photogenerated electron-hole pairs. In this experiment, BiOI combined with $SnO_2$/NCQDs composite by in situ method to obtain $SnO_2$/NCQDs/BiOI composite. NCQDs and BiOI can form nanojunctions, which were proved to enhance the photocatalytic activity of BiOI [30–33]. Hence, the PEC immunosensor based on $SnO_2$/NCQDs/BiOI composite with excellent photochemical properties was constructed, which could achieve ultrasensitive detection of cardiac troponin I (cTnI). Cardiac troponin I is a specific indicator of myocardial injury, and its diagnostic specificity could be used to diagnose unstable angina pectoris [34, 35]. An increase in the level of cTnI often portended a higher risk of short-term death, so continuous measurement of cTnI level was crucial to prevent myocardial infarction [36–40]. Hence, a new type PEC immunosensor was developed based on NCQDs and BiOI co-sensitized $SnO_2$ microflowers for cTnI detection. First, the anti-cTnI was immobilized on $SnO_2$/NCQDs/BiOI-modified ITO electrode, and then bovine serum albumin (BSA) was used to block the nonspecific binding sites. Therefore, different concentrations of cTnI were dropped on the electrodes to form a sensitive PEC platform for cTnI detection.

## Experimental section

### Reagents and materials

Indium tin oxide (ITO) glass obtained by Zhuhai Kaivo Electronic Components Co., Ltd. (Zhuhai, China) was used as a working electrode. Tin tetrachloride and potassium iodide were provided by Shanghai Macklin Biochemical Co., Ltd. (Shanghai, China). Isopropanol was obtained from Tianjin Fuyu Fine Chemical Co., Ltd. (Tianjin, China). Sodium sulfide was purchased from Tianjin Komeio Chemical Reagent Co., Ltd. (Tianjin, China). The other details are provided in Electronic Supplementary Material (ESM†).

All PEC experiments were tested on CHI760E electrochemical workstation (Shanghai Chenhua Instruments Co., Ltd., China) with a three-electrode system including an ITO working electrode, a platinum wire electrode as counter electrode, and a saturated calomel electrode as reference electrode. A 100 W LED lamp (white light) was used as an irradiation source in the PEC test. The other details are given in ESM†.

### The synthesis of flower-like $SnO_2$ and NCQDs

Flower-like $SnO_2$ was prepared by hydrothermal synthesize method [18], and NCQDs was prepared by the previous work according to the literature [41].

### The construction process of the PEC immunosensor

Preparatory works of required materials and reagents were as follows. The ITO electrodes (2.5 × 0.8 $cm^2$) were cleaned with an aqueous solution mixed with cleanser essence, acetone, ethanol, and ultrapure water, respectively. The cleaned ITO electrodes were dried in oven (70 °C) for 2 h, naturally cooled for further use. Phosphate buffer saline (PBS) with different pH values (pH 5.8–8.8) were prepared by mixing disodium hydrogen phosphate ($Na_2HPO_4$, 1/15 mol·$L^{-1}$), potassium dihydrogen phosphate ($KH_2PO_4$, 1/15 mol·$L^{-1}$), and ultrapure water in different proportions. Several concentrations of cTnI and 1 μg·$mL^{-1}$ anti-cTnI were prepared with PBS buffer (pH = 7.4) and stored in thermostatic refrigerator (4 °C) for later use.

Figure 1 shows the construction process of the PEC immunosensor. Firstly, 10 μL of $SnO_2$ suspension (3 mg $mL^{-1}$) was accurately transferred to a clean ITO electrode to form ITO/$SnO_2$ electrode, which was placed in a muffle furnace (500 °C) for 30 min, naturally cooled. A total of 3 μL of NCQDs solution (1 mol $L^{-1}$) was dropped on the ITO/$SnO_2$ electrode, which was dried at room temperature and then washed with ultrapure water to remove excess NCQDs. Subsequently, 3 μL of 0.06 mol $L^{-1}$ $Bi(NO_3)_3$ dilute nitric acid solution and 0.01 mol $L^{-1}$ KI solution were modified to the surface of ITO/$SnO_2$/NCQDs electrode, respectively. Rinsing with anhydrous ethanol, the ITO/$SnO_2$/NCQDs/BiOI was successfully prepared. Whereafter, 3 μL of 0.1 mol $L^{-1}$ dopamine (DA) tris-HCl (pH 8.5) solution was dropped onto the surface of ITO/$SnO_2$/NCQDs/BiOI electrode for 30 min to form polydopamine (PDA) by the self-polymerization of dopamine molecules. DA had a unique molecular structure, similar to mussels' adhesion proteins: catechol and amine functional groups. In weakly alkaline aqueous solution (pH 8.5), DA easily self-polymerized to form PDA.

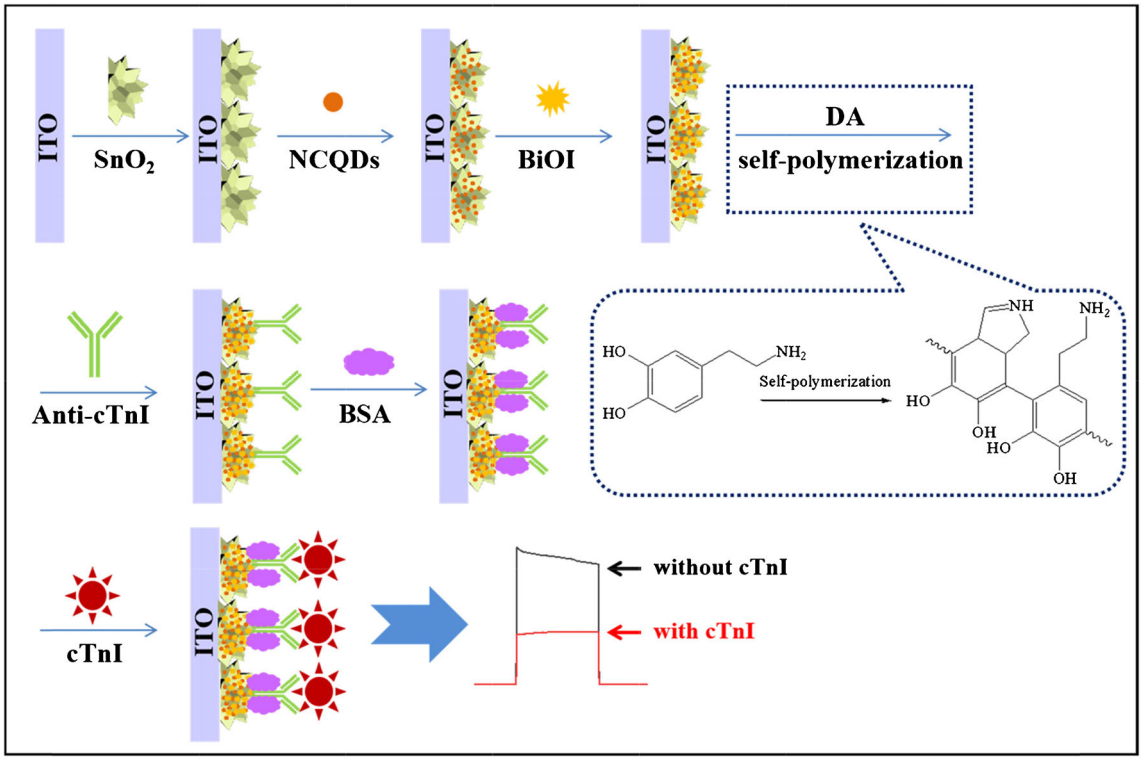


**Fig. 1** Construction process of the ultrasensitive PEC immunosensor based on $SnO_2$/NCQDs/BiOI composite for cTnI detection

Due to the strong adhesion of PDA, many biomolecules could be immediately attached to the surface of the PDA [42, 43]. Hence, 3 μL of anti-cTnI (1 μg $mL^{-1}$) was attached to PDA, and excess of BSA (1 mg $mL^{-1}$) was used to block the non-specific binding site on anti-cTnI. Finally, different concentrations of cTnI were dropped to the above electrodes by specific junctions of antigenic antibodies. Therefore, the PEC immunosensor was successfully constructed.

## Results and discussion

### Characterization of $SnO_2$, $SnO_2$/NCQDs, and $SnO_2$/NCQDs/BiOI materials

In this experiment, the morphologies and elements analyze of $SnO_2$, $SnO_2$/NCQDs, and $SnO_2$/NCQDs/BiOI by scanning electron microscope (SEM) and transmission electron microscope (TEM) are shown in Fig. 2. The morphology of $SnO_2$ (Fig. 2 a and b) has rich mesoporous structure, which could provide a large number of binding sites to bind other nanomaterials with very small particle size. NCQDs had abundant carboxy groups, so it was easier to combine with $SnO_2$. From Fig. 2c, the lamella of $SnO_2$ microflower became thicker when NCQDs was modified on $SnO_2$, which indicated that NCQDs successfully combined with $SnO_2$. SEM (Fig. 2d) and TEM (Fig. 2e; Fig. S1A) images indicated that the structure of $SnO_2$/NCQDs/BiOI was similar to $SnO_2$, which retained the same mesoporous flower-like structure. The difference was that a mass of small nanoparticles attached to the surface of $SnO_2$/NCQDs composite. Combined with the EDS image (Fig. 2f) and the TEM relevant mapping image (Fig. S1B to Fig. S1F) of $SnO_2$/NCQDs/BiOI, it was observed that the elements Sn, O, N, Bi, and I were all detected. As the TEM operation of this process was carried out on a spraying carbon copper mesh, no element C was added in Fig. S1.

The X-ray diffraction (XRD) pattern of $SnO_2$, $SnO_2$/NCQDs, and $SnO_2$/NCQDs/BiOI is demonstrated in Fig. 3a. The XRD curve of flower-like $SnO_2$ was matched well with the rutile tetragonal phase $SnO_2$ (PDF#41-1445). As a small quantity of NCQDs and BiOI was modified on $SnO_2$ layer by layer, the main peak of $SnO_2$ unchanged. The peak position of BiOI matched well with PDF#02-0634, which could be found on the curve of $SnO_2$/NCQDs/BiOI composite [44–46]. From Fig. 3b, the UV-vis diffuse reflectance of the prepared materials was revealed. The pure $SnO_2$ with wide band gap (3.60 eV) (Fig. 3c) exhibited the weak absorption ability in visible light region (Fig. 3b, curve a). NCQDs combined with $SnO_2$ increased the absorption intensity (Fig. 3b, curve b) and the utilization rate of visible light could be improved. Furthermore, BiOI with narrow band gap (1.83 eV, Fig. 3d) was modified on NCQDs sensitized $SnO_2$ to form $SnO_2$/NCQDs/BiOI composite, which had the strongest absorption ability in visible region (Fig. 3b, curve c).

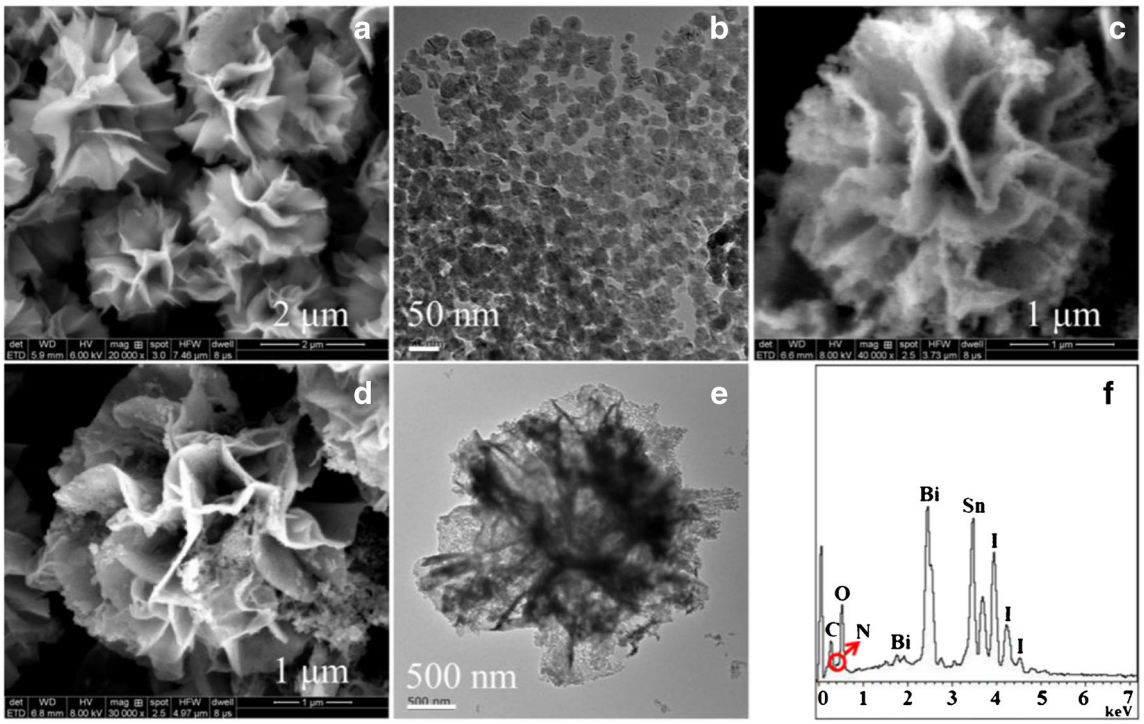


**Fig. 2** The SEM images of **a** $SnO_2$, **c** $SnO_2$/NCQDs, and **d** $SnO_2$/NCQDs/BiOI. The TEM images of **b** $SnO_2$ with mesoporous structure and **e** $SnO_2$/NCQDs/BiOI. The EDS image of **f** $SnO_2$/NCQDs/BiOI

## Characterization of the prepared PEC immunosensor

The successful construction of ultrasensitive PEC immunosensor was demonstrated by photocurrent measurement (Fig. 4a) and electrochemical impedance spectroscopy (EIS) method (Fig. 4b) through layer-by-layer assembly. From Fig. 4a, the photocurrent of unloaded ITO electrode was about 0 μA (curve a). The photocurrent response of ITO/$SnO_2$ (curve b) and ITO/$SnO_2$/NCQDs (curve c) electrodes had been improved to some extent due to the successive

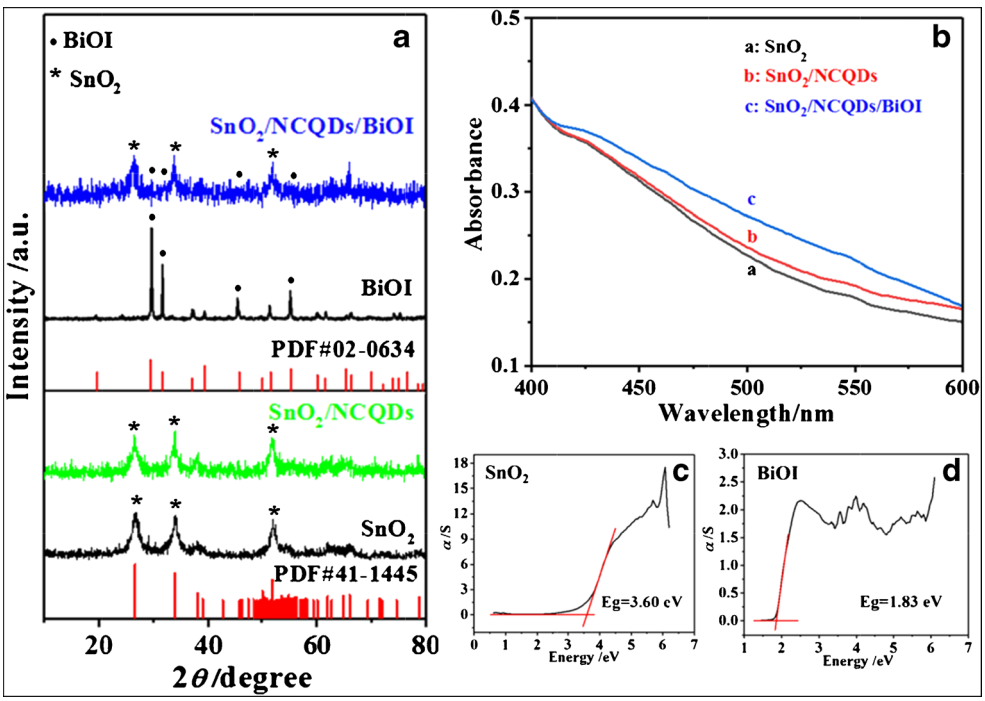


**Fig. 3** **a** XRD image of $SnO_2$, $SnO_2$/NCQDs, $SnO_2$/NCQDs/BiOI, and BiOI; **b** UV-vis diffuse reflectance spectra images of $SnO_2$, $SnO_2$/NCQDs, and $SnO_2$/NCQDs/BiOI; The band gap images of **c** $SnO_2$ and **d** BiOI

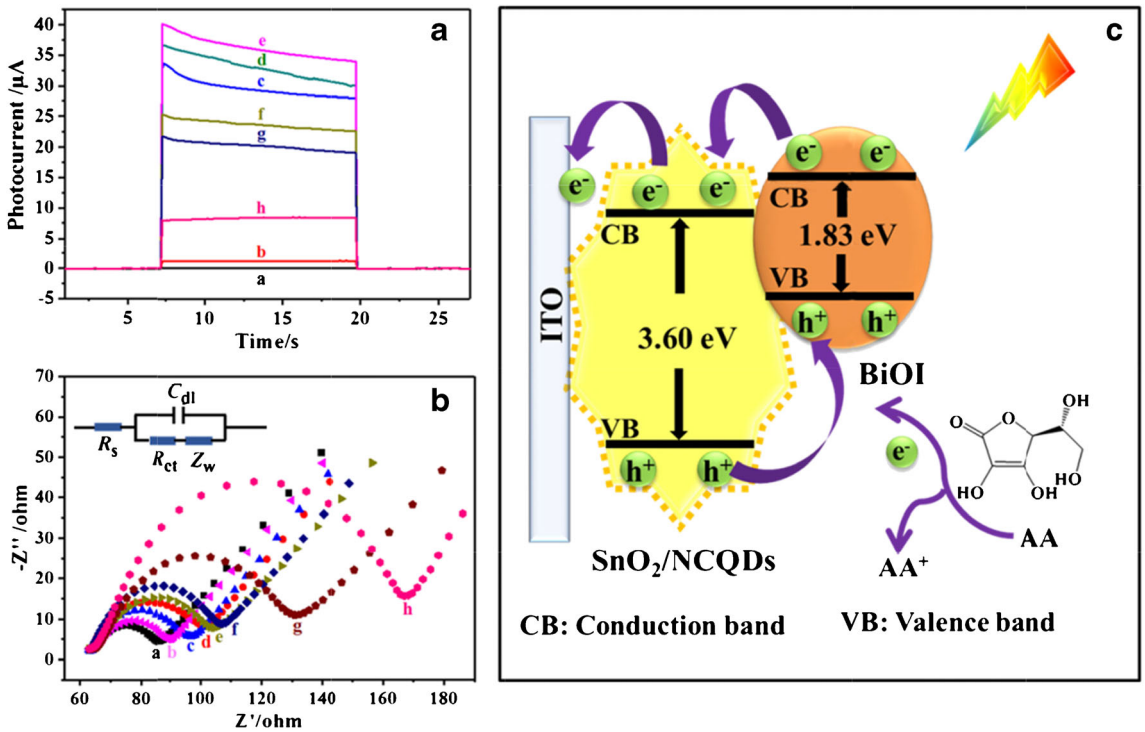


**Fig. 4** **a** Photocurrent variation trend and **b** EIS Nyquist curves during the construction of ultrasensitive PEC immunosensor through layer-by-layer assembly: (a) ITO, (b) ITO/$SnO_2$, (c) ITO/$SnO_2$/NCQDs, (d) ITO/$SnO_2$/NCQDs/BiOI, (e) ITO/$SnO_2$/NCQDs/BiOI/PDA, (f) ITO/$SnO_2$/NCQDs/BiOI/PDA/anti-cTnI, (g) ITO/$SnO_2$/NCQDs/BiOI/PDA/anti-cTnI/BSA, (h) ITO/$SnO_2$/NCQDs/BiOI/PDA/anti-cTnI/BSA/cTnI. Inset figure of **b**: the electrical equivalent circuit applied to fit the impedance spectra. The concentration of cTnI was 1 ng $mL^{-1}$ and the applied potential was 0 V. **c** The electron-transfer mechanism of the PEC sensor based on $SnO_2$/NCQDs/BiOI composite in PBS electrolyte containing AA for cTnI detection

modification of $SnO_2$ and NCQDs on the ITO electrode. After BiOI nanoparticles grew on the surface of above electrode through in-situ growth method, the photocurrent changed significantly (curve d) from around 1 to 33 μA. Herein, NCQDs acted as a linker in the in-situ growth of BiOI on $SnO_2$ microflower. After DA formed to PDA via self-polymerization on the ITO/$SnO_2$/NCQDs/BiOI electrode, the photocurrent improved to 35 μA (curve e). This phenomenon could be attributed to the reduction of the phenolic hydroxyl groups on the surface of the PDA, which helped to reduce photogenerated holes and achieved the separation photogenerated holes/electrons. As anti-cTnI (curve f), BSA (curve g), and cTnI (curve h) were successively modified on the above electrode, the photocurrent signal gradually decreased. As protein molecules, anti-cTnI, BSA, and cTnI had a certain insulating property, which inhibited $e^-$ from AA to the photosensitive matrix and hinder the transmission of photon-generated carrier. What is more, the photocurrent intensity decreased again after anti-cTnI binding to cTnI. Hence, the construction of this ultrasensitive PEC immunosensor through layer-by-layer assembly was successful.

EIS method was carried out to further confirm the successful construction of the PEC immunosensor (Fig. 4b). The electrode was immersed in a mixture solution containing KCl (5.0 mmol $L^{-1}$) and $[Fe(CN)_6]^{3-/4-}$ (0.10 mol $L^{-1}$) throughout the process. Inset in Fig. 4b indicates the equivalent circuit, which included four parts: the ohmic resistance of the electrolyte solution ($R_s$), the Warburg impedance ($Z_w$), the interfacial double layer capacitance ($C_{dl}$), and the electron transfer resistance ($R_{et}$). The unloaded ITO electrode showed a very small $R_{et}$ value (curve a). The $R_{et}$ value gradually increased as $SnO_2$ (curve b), NCQDs (curve c), and BiOI (curve d) were modified on the unloaded ITO electrode in sequence. The $R_{et}$ value further increased after PDA on ITO/$SnO_2$/NCQDs/BiOI electrode (curve e). PDA generated organic molecular membrane on the surface of above electrode, which could hinder electron transfer. Since proteins were nonconductive and blocked electron transport, the $R_{et}$ value was gradually increased after modification with anti-cTnI (curve f), BSA (curve g), and cTnI (curve h) on above electrode in turn. Hence, the gradual increase of $R_{et}$ value indicated that the ultrasensitive PEC immunosensor had been constructed successfully and could be used for cTnI detection.

The electron transfer of the ultrasensitive PEC immunosensor in AA electrolyte is shown in Fig. 4c. $SnO_2$

was used as the photosensitive matrix, NCQDs/BiOI photoactive nanocomposites were used as sensitizers. $SnO_2$ had wide band gap of 3.60 eV, which limited its visible light absorption ability. However, because of its good biocompatibility, high stability, and environmental protection, $SnO_2$ was used as excellent electrode material. NCQDs was modified on $SnO_2$ could enhance the PEC response. NCQDs had absorption activity under visible light, which was beneficial to improving the absorption of $SnO_2$ to visible light and could enhance photocatalytic performance. Therefore, NCQDs modified on $SnO_2$ could enhance the PEC response [47]. $SnO_2$ and BiOI could be stimulated to generate $e^-/h^+$ pairs, the photo-induced electrons on the valence band (VB) of BiOI flowed into its conduction band (CB), then transfused to the CB of $SnO_2$. The strong PEC response furnished a basic for successful construction and high detection sensitivity of the ultrasensitive PEC immunosensor for cTnI detection.

## Optimization of method

The following parameters were optimized: (a) concentration of Bi(III) (Fig. S2A), (b) concentration of AA (Fig. S2B), and (c) pH value of PBS buffer (Fig. S2C). Respective text and figures on optimization are given in the Electronic Supporting Material. It was worth mentioning that excessive amounts of AA (> 0.1 mol $L^{-1}$) could cause the decrease of photocurrent, at high AA concentration, the reduction of photocurrent could be attributed to the absorption of quencher solution, thus reduced the irradiation intensity and efficiency of the excited electron hole center [48]. In short, the following experimental conditions were found to give best results: (a) optimal Bi(III) concentration was 0.06 mol $L^{-1}$, (b) optimal concentration of AA was 0.1 mol $L^{-1}$, and (c) the best pH value of PBS buffer was 8.0.

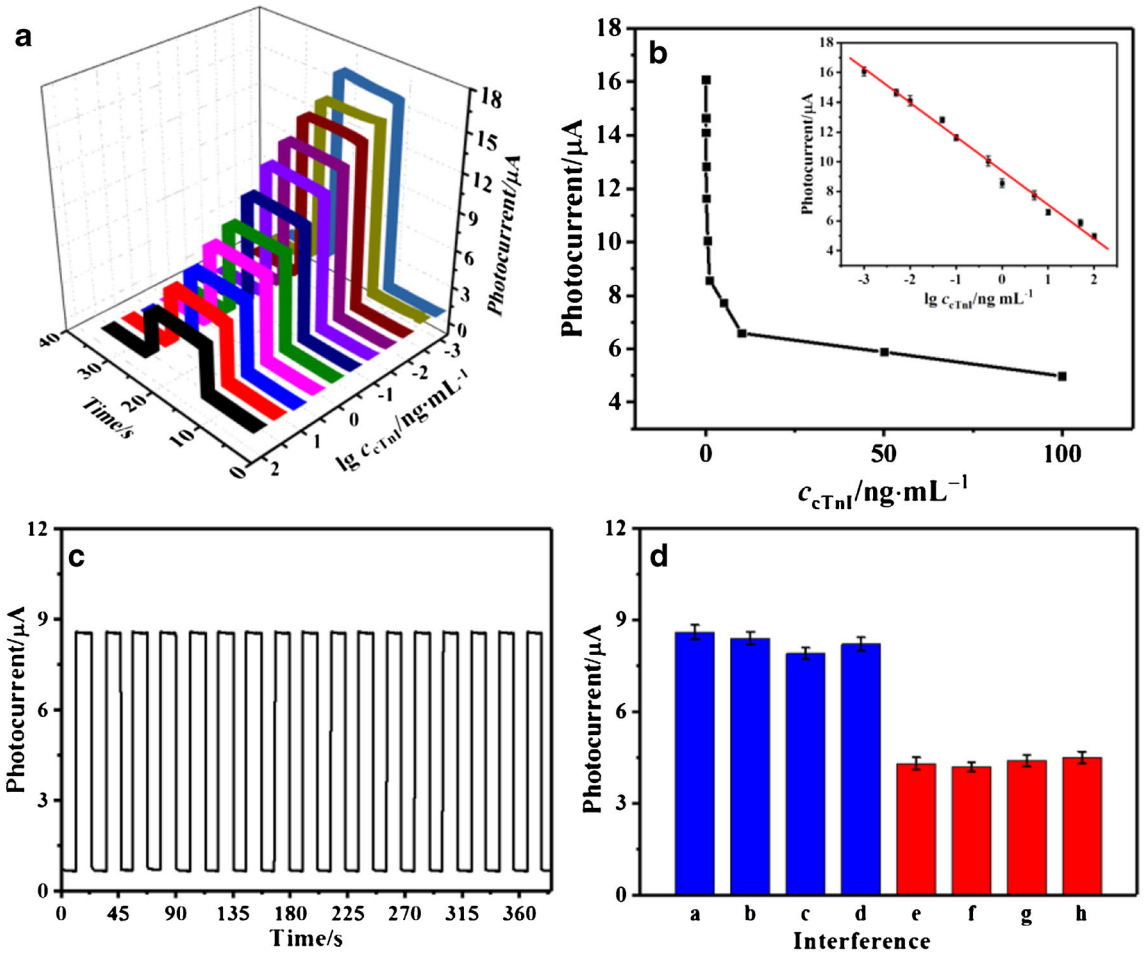


**Fig. 5** **a** The working curve and **b** the relevant logarithmic curve of the PEC immunosensor under conditions of $SnO_2$ (3.0 mg $mL^{-1}$), NCQDs (1 mg $mL^{-1}$), $Bi(NO_3)_3$ (0.06 mol $L^{-1}$), KI (0.01 mol $L^{-1}$), and AA with 0.1 mol $L^{-1}$ in pH 8.0 PBS buffer. The concentration of cTnI was 0.001 to 100 ng $mL^{-1}$. **c** The stability measurement of PEC immunosensor ($c_{cTnI}$ = 1 ng·$mL^{-1}$) at 400 s on/off light cycles. **d** The selectivity text of PEC immunosensor for cTnI detection (a) Blank, (b) Blank + CEA (100 ng $mL^{-1}$), (c) Blank + SCCA (100 ng $mL^{-1}$), (d) Blank + H-IgG (100 ng $mL^{-1}$), (e) cTnI (0.1 ng $mL^{-1}$), (f) cTnI (1 ng $mL^{-1}$) + CEA (100 ng $mL^{-1}$), (g) cTnI (1 ng $mL^{-1}$) + SCCA (100 ng $mL^{-1}$), (h) cTnI (1 ng $mL^{-1}$) + H-IgG (100 ng $mL^{-1}$). The applied potential was 0 V

**Table 1** Different detection methods for cTnI

| Technique | Materials | Linear range (ng $mL^{-1}$) | Detection limit (pg $mL^{-1}$) | Reference |
|---|---|---|---|---|
| PEC immunosensor | $SnO_2$/NCQDs/BiOI | 0.001–100 | 0.3 | This method |
| Immunosensor | Amine functionalized graphene | 0.01–1 | 10 | [50] |
| Fluorescent aptasensor | Graphene oxide | 0.1–6 | 70 | [51] |
| Surface plasmon resonance (SPR) biosensing | $Fe_3O_4$@PDA immune probe | 15–2500 | 3750 | [52] |
| Immunoassay | Fluoro-microbead guiding chip | 0.1–100 | 41 | [53] |
| Voltammetric aptasensor | Magnetic metal-organic framework | 0.01–100 | 5.7 | [54] |
| Dendrimer enhanced impedimetric immunosensor | Tetramethylbenzidine | 0.001–1000 | 0.0117 | [40] |
| Self-accelerated electrochemiluminescence emitters | Ag@$SnO_2$ nanoflowers | $1 \times 10^{-6}$–0.1 | $0.11 \times 10^{-3}$ | [34] |
| Electrochemical sandwich immunosensor | Nitrogen/sulfur co-doped graphene oxide modified with Au@Ag nanocubes | $0.1 \times 10^{-3}$–250 | 0.033 | [35] |

## PEC analysis for cTnI

The working curve (Fig. 5a) and the logarithm fitting curve (Fig.5b) reflected the performance of the PEC immunosensor, which displayed the photocurrent corresponding to various concentrations of cTnI (0.001–100 ng $mL^{-1}$). The linear equation was $I = 9.392–2.295\lg c_{cTnI}$, and the linear coefficient was 0.998. On the basis of the previous literature [49], the detection limit was 0.3 pg $mL^{-1}$ by calculation. Hence, the prepared PEC immunosensor had wider detection range and lower detection limit compared with other detect methods of cTnI (Table 1). Besides, the reproducibility evaluation of the prepared PEC immunosensor ($c_{cTnI} = 1$ ng $mL^{-1}$) were investigated utilizing five electrodes. Under the same conditions, five electrodes (8.56 μA, 8.47 μA, 8.55 μA, 8.52 μA, 8.59 μA) were detected, and the relative standard deviation (RSD) was about 4.55%.

A PEC immunosensor with excellent performance, good stability, reproducibility, and selectivity was essential. In a stability test of the immunosensor under 400 s on/off circulation, the photocurrent has no obvious change (Fig. 5b). The result of the selectivity test of the immunosensor is shown in Fig. 5d; no obvious photocurrent change was discovered after 100 ng $mL^{-1}$ of carcinoembryonic antigen (CEA), squamous cell carcinoma antigen (SCCA), and human immunoglobulin antigen (H-IgG), which were modified on the blank electrode (ITO/$SnO_2$/NCQDs/BiOI/PDA/Anti-cTnI/BSA) either mixed with cTnI or not, respectively. Therefore, the PEC immunosensor had great selectivity and specificity for the determination of cTnI.

## Application of the PEC immunosensor in human serum

Using the standard addition method, various concentrations of cTnI were added into human serum samples to analyze the practicability of the PEC immunosensor. The genuine serum samples were obtained from the University of Jinan Hospital (Jinan, China). Before the measurement, the genuine serum sample was centrifuged at 2800 rpm for 10 min under 4 °C, and the supernate was received as the detection sample. When cTnI levels in genuine serum samples were found to exceed the calibration range, they were then diluted appropriately with 1/15 mol $L^{-1}$ PBS buffer (pH 7.4). After obtained the real sample (0.70 ng·$mL^{-1}$), a standard concentration of cTnI with 0.50, 1.00, and 5.00 ng $mL^{-1}$ was added to the obtained sample, respectively. Using standardized recycling method, traditional three-electrode system (saturated calomel electrode

**Table 2** The testing results of cTnI-spiked human blood serum samples

| Content of cTnI in serum sample (ng $mL^{-1}$) | Added content of cTnI (ng $mL^{-1}$) | The detection content (ng $mL^{-1}$, $n = 5$) | RSD (%, $n = 5$) | Recovery (%) |
|---|---|---|---|---|
| 0.70 | 0.50 | 1.27, 1.21, 1.20, 1.23, 1.19 | 3.16 | 104 |
| | 1.00 | 1.73, 1.67, 1.73, 1.68, 1.74 | 3.24 | 101 |
| | 5.00 | 5.70, 5.62, 5.69, 5.68, 5.71 | 3.54 | 99.6 |

(SCE) for reference, platinum electrode for counter) was used for measuring the PEC response in 10 mL of PBS (pH 7.4) buffer dissolving 0.1 mol $L^{-1}$ AA. To further analyze the accuracy of the immunosensor, a recognized ELISA method was compared with the designed PEC immunosensor (Table S2). When the confidence coefficient $\alpha$ was 0.05, the calculated $F$ was less than $F_f$ ($F = 2.24$, $F_f = 6.39$) and the calculated $t$ value was less than $t$, $F$ ($t = 0.222$, $F = 2.31$), which fully proved that the designed PEC immunosensor had excellent feasibility and accuracy. From Table 2, the calculated RSD of the prepared PEC immunosensor was 3.16–3.54%, while the range of recovery was 99.6–104%. Therefore, the PEC immunosensor owned excellent feasibility and veracity.

## Conclusion

To sum up, an ultrasensitive PEC immunosensor was triumphantly established for detection of cTnI on the basis of $SnO_2$/NCQDs/BiOI composite. The NCQDs and BiOI co-sensitized structure effectively promote the electron transfer and enhanced the use rate of visible light, which achieved excellent PEC response and sensitivity of the immunosensor. In addition, AA was designed as electrode donor, which eliminated the photogenerated holes and further enhanced the photocurrent and increased the sensitivity of the immunosensor. This novel and ultrasensitive PEC immunosensor achieve high sensitivity to cTnI detection with a wide liner and a low detection limit. Furthermore, excellent stability and satisfactory reproducibility was also been owned of the immunosensor for sensitive cTnI detection, which had a broad application prospect in the fields of early diagnosis of cardiovascular disease.

**Funding information** This research was financially supported by the Innovation team project of colleges and universities in Jinan (No. 2019GXRC027), the National Natural Science Foundation of China (Nos. 21775054, 21775053, 21575050, 21777056, 21505051), the National Key Scientific Instrument and Equipment Development Project of China (No. 21627809), the Natural Science Foundation of Shandong Province (No. ZR2017MB027), and the Jinan Scientific Research Leader Workshop Project (2018GXRC024).

### Compliance with ethical standards

**Conflict of interest** The authors declare that they have no competing interests

## References

1. Fan BB, Fan Q, Cui M, Wu TT, Wang JS, Ma HM, Wei Q (2019) Photoelectrochemical biosensor for sensitive detection of soluble CD44 based on the facile construction of a poly(ethylene glycol)/hyaluronic acid hybrid antifouling interface. ACS Appl Mater Interfaces 11:24764–24770. https://doi.org/10.1021/acsami.9b06937
2. Chen Y, Zhou YL, Yin HS, Li F, Li H, Guo RZ, Han YH, Ai SY (2020) Photoelectrochemical biosensor for histone acetyltransferase detection based on ZnO quantum dots inhibited photoactivity of BiOI nanoflower. Sensors Actuators B Chem 307:127633. https://doi.org/10.1016/j.snb.2019.127633
3. Wang J, Lv WX, Wu JH, Li HY, Li F (2019) Electropolymerization-induced positively charged phenothiazine polymer photoelectrode for highly sensitive photoelectrochemical biosensing. Anal Chem 91(21):13831–13837. https://doi.org/10.1021/acs.analchem.9b03311
4. Yi WJ, Cai RL, Xiang DF, Wang YX, Zhang MS, Ma QH, Cui YH, Bian XU (2019) A novel photoelectrochemical strategy based on an integrative photoactive heterojunction nanomaterial and a redox cycling amplification system for ultrasensitive determination of microRNA in cells. Biosens Bioelectron 143:111614. https://doi.org/10.1016/j.bios.2019.111614
5. Bao CZ, Fan DW, Liu X, Wang XY, Wu D, Ma HM, Hu LH, Wang H, Sun X, Wei Q (2019) A signal-off type photoelectrochemical immunosensor for the ultrasensitive detection of procalcitonin: $Ru(bpy)_3(2+)$ and $Bi_2S_3$ co-sensitized $ZnTiO_3$/$TiO_2$ polyhedra as matrix and dual inhibition by $SiO_2$/PDA-Au. Biosens Bioelectron 142:111513. https://doi.org/10.1016/j.bios.2019.111513
6. Tan JS, Peng B, Tang L, Feng CY, Wang JJ, Yu JF, Ouyang XL, Zhu X (2019) Enhanced photoelectric conversion efficiency: a novel h-BN based self-powered photoelectrochemical aptasensor for ultrasensitive detection of diazinon. Biosens Bioelectron 142:111546. https://doi.org/10.1016/j.bios.2019.111546
7. Cao Y, Wang LN, Wang CY, Hu XY, Liu YL, Wang GX (2019) Sensitive detection of glyphosate based on a Cu-BTC MOF/g-$C_3N_4$ nanosheet photoelectrochemical sensor. Electrochim Acta 317:341–347. https://doi.org/10.1016/j.electacta.2019.06.004
8. Liu X, Fan DW, Duan SQ, Bao CZ, Wang H, Wang XY, Sun X, Wei Q (2019) An ultrasensitive label-free photoelectrochemical sensor based on $Ag_2O$-sensitized $WO_3$/$TiO_2$ acicular composite for AFB1 detection. Anal Methods 11(30):3890–3897. https://doi.org/10.1039/C9AY01277J
9. Yang RY, Zou K, Zhang XH, Du CC, Chen JH (2019) Target-induced photocurrent-polarity switching: a highly selective and sensitive photoelectrochemical sensing platform. Chem Commun 55(61):8939–8942. https://doi.org/10.1039/C9CC03973B
10. Wang S, Li SP, Wang WW, Zhao MZ, Liu JF, Feng HF, Chen YM, Gu Q, Du Y, Hao WC (2019) A non-enzymatic photoelectrochemical glucose sensor based on $BiVO_4$ electrode under visible light. Sensors Actuators B Chem 291:34–41. https://doi.org/10.1016/j.snb.2019.04.057
11. Wang HH, Li MJ, Wang HJ, Chai YQ, Yuan R (2019) P-n-sensitized heterostructure $Co_3O_4$/fullerene with highly efficient photoelectrochemical performance for ultrasensitive DNA detection. ACS Appl Mater Interfaces 11(26):23765–23772. https://doi.org/10.1021/acsami.9b05923
12. Shang MX, Zhang JL, Qi H, Gao Y, Yan JY, Song WB (2019) All-electrodeposited amorphous MoSx@ZnO core-shell nanorod arrays for self-powered visible-light-activated photoelectrochemical tobramycin aptasensing. Biosens Bioelectron 136:53–59. https://doi.org/10.1016/j.bios.2019.04.019
13. Tolba SA, Allam NK (2019) Computational design of novel hydrogen-doped, oxygen-deficient monoclinic zirconia with excellent optical absorption and electronic properties. Sci Rep 9(1):10159. https://doi.org/10.1038/s41598-019-46778-5
14. Chen X, Huang Y, Zhang K (2018) Cobalt nanofibers coated with layered nickel silicate coaxial core-shell composites as excellent anode materials for lithium ion batteries. J Colloid Interface Sci 513:788–796. https://doi.org/10.1016/j.jcis.2017.11.078

15. Tian YZ, Wang Q, Shen L, Cui ZC, Kou LJ, Cheng J, Zhang J (2019) A renewable resveratrol-based epoxy resin with high Tg, excellent mechanical properties and low flammability. Chem Eng J : 123124. https://doi.org/10.1016/j.cej.2019.123124
16. Zhang B, Ma J, Ye J, Jin YJ, Yang CY, Ding JJ, Zhang ZG, Hou ZP, Liu Q, Ye F (2019) Ultra-low cost porous mullite ceramics with excellent dielectric properties and low thermal conductivity fabricated from kaolin for radome applications. Ceram Int 45(15): 18865–18870. https://doi.org/10.1016/j.ceramint.2019.06.120
17. Ma W, Hu K, Chen Q, Zhou M, Mirkin MV, Bard AJ (2017) Electrochemical size measurement and characterization of electrodeposited platinum nanoparticles at nanometer resolution with scanning electrochemical microscopy. Nano Lett 17(7):4354–4358. https://doi.org/10.1021/acs.nanolett.7b01437
18. Fan DW, Bao CZ, Liu X, Wu D, Zhang Y, Wang H, Du B, Wei Q (2018) A novel label-free photoelectrochemical immunosensor based on NCQDs and $Bi_2S_3$ co-sensitized hierarchical mesoporous $SnO_2$ microflowers for detection of NT-proBNP. J Mater Chem B 6(46):7634–7642. https://doi.org/10.1039/C8TB02122H
19. Lee PM, Liao CH, Lin CH, Liu CY (2018) Photocurrent generation in $SnO_2$ thin film by surface charged chemisorption O ions. Appl Surf Sci 442:398–402. https://doi.org/10.1016/j.apsusc.2018.01.289
20. Kamarulzaman N, Abdul Aziz ND, Kasim MF, Chayed NF, Yahaya Subban RH, Badar N (2019) Anomalies in wide band gap $SnO_2$ nanostructures. J Solid State Chem 277:271–280. https://doi.org/10.1016/j.jssc.2019.05.035
21. Yang XL, Yu Q, Zhang SF, Sun P, Lu HY, Yan X, Liu FM, Zhou X, Liang XS, Gao Y, Lu GY (2018) Highly sensitive and selective triethylamine gas sensor based on porous $SnO_2/Zn_2SnO_4$ composites. Sens Actuators B Chem 266:213–220. https://doi.org/10.1016/j.snb.2018.03.044
22. Li YY, Wang JG, Sun HH, Hua W, Liu XR (2018) Heterostructured $SnS_2/SnO_2$ nanotubes with enhanced charge separation and excellent photocatalytic hydrogen production. Int J Hydrog Energy 43(31):14121–14129. https://doi.org/10.1016/j.ijhydene.2018.05.130
23. Liu S, Gao S, Wang ZW, Fei T, Zhang T (2019) Oxygen vacancy modulation of commercial $SnO_2$ by an organometallic chemistry-assisted strategy for boosting acetone sensing performances. Sens Actuators B Chem 290:493–502. https://doi.org/10.1016/j.snb.2019.03.123
24. Yang JS, Wu HX, Yang P, Hou CJ, Huo DQ (2018) A high performance N-doped carbon quantum dots/5,5′-dithiobis-(2-nitrobenzoic acid) fluorescent sensor for biothiols detection. Sens Actuators B Chem 255:3179–3186. https://doi.org/10.1016/j.snb.2017.09.143
25. Pang XH, Zhang Y, Pan J, Zhao Y, Chen Y, Ren X, Ma HM, Wei Q, Du B (2016) A photoelectrochemical biosensor for fibroblast-like synoviocyte cell using visible light-activated NCQDs sensitized-ZnO/$CH_3NH_3PbI_3$ heterojunction. Biosens Bioelectron 77: 330–338. https://doi.org/10.1016/j.bios.2015.09.047
26. Kim SR, Jo WK (2019) Boosted photocatalytic decomposition of nocuous organic gases over tricomposites of N-doped carbon quantum dots, $ZnFe_2O_4$, and BiOBr with different junctions. J Hazard Mater 380:120866. https://doi.org/10.1016/j.jhazmat.2019.120866
27. Zhang JJ, Wang ZB, Li C, Zhao L, Liu J, Zhang LM, Gu DM (2015) Multiwall-carbon nanotube modified by N-doped carbon quantum dots as Pt catalyst support for methanol electrooxidation. J Power Sources 289:63–70. https://doi.org/10.1016/j.jpowsour.2015.04.150
28. Jiang ZY, Liang XZ, Liu YY, Jing TJ, Wang ZY, Zhang XY, Qin XY, Dai Y, Huang BB (2017) Enhancing visible light photocatalytic degradation performance and bactericidal activity of BiOI via ultrathin-layer structure. Appl Catal B Environ 211:252–257. https://doi.org/10.1016/j.apcatb.2017.03.072
29. Wang XW, Zhang Y, Zhou CX, Huo DZ, Zhang RB, Wang LZ (2019) Hydroxyl-regulated BiOI nanosheets with a highly positive valence band maximum for improved visible-light photocatalytic performance Appl Catal B Environ : 118390. https://doi.org/10.1016/j.apcatb.2019.118390, , 268
30. Zhu YH, Liu X, Yan K, Zhang JD (2019) A cathodic photovoltammetric sensor for chloramphenicol based on BiOI and graphene nanocomposites. Sens Actuators B Chem 284:505–513. https://doi.org/10.1016/j.snb.2018.12.160
31. Chen DM, Yang JJ, Zhu Y, Zhang YM, Zhu YF (2018) Fabrication of BiOI/graphene Hydrogel/FTO photoelectrode with 3D porous architecture for the enhanced photoelectrocatalytic performance. Appl Catal B Environ 233:202–212. https://doi.org/10.1016/j.apcatb.2018.04.004
32. Zhong S, Wang BQ, Zhou H, Li CY, Peng XJ, Zhang SY (2019) Fabrication and characterization of Ag/BiOI/GO composites with enhanced photocatalytic activity. J Alloys Compd 806:401–409. https://doi.org/10.1016/j.jallcom.2019.07.223
33. Liu ZY, Wang QY, Tan XY, Wang YJ, Jin RC, Gao SM (2019) Enhanced photocatalytic performance of $TiO_2$ NTs decorated with chrysanthemum-like BiOI nanoflowers. Sep Purif Technol 215: 565–572. https://doi.org/10.1016/j.seppur.2019.01.046
34. Jiang MH, Lu P, Lei YM, Chai YQ, Yuan R, Zhuo Y (2018) Self-accelerated electrochemiluminescence emitters of Ag@$SnO_2$ nanoflowers for sensitive detection of cardiac troponin T. Electrochim Acta 271:464–471. https://doi.org/10.1016/j.electacta.2018.03.177
35. Lv H, Zhang XB, Li YY, Ren Y, Zhang CY, Wang P, Xu Z, Li XJ, Chen ZW, Dong YH (2019) An electrochemical sandwich immunosensor for cardiac troponin I by using nitrogen/sulfur co-doped graphene oxide modified with Au@Ag nanocubes as amplifiers. Microchim Acta 186:416. https://doi.org/10.1007/s00604-019-3526-2
36. Bohlooli Ghashghaee N, Tanner BCW, Dong WJ (2017) Functional significance of C-terminal mobile domain of cardiac troponin I. Arch Biochem Biophys 634:38–46. https://doi.org/10.1016/j.abb.2017.09.017
37. Burkart EM, Sumandea MP, Kobayashi T, Nili M, Martin AF, Homsher E, Solaro RJ (2003) Phosphorylation or glutamic acid substitution at protein kinase C sites on cardiac troponin I differentially depress myofilament tension and shortening velocity. J Biol Chem 278(13):11265–11272. https://doi.org/10.1074/jbc.M210712200
38. Bottenus D, Hossan MR, Ouyang Y, Dong WJ, Dutta P, Ivory CF (2011) Preconcentration and detection of the phosphorylated forms of cardiac troponin I in a cascade microchip by cationic isotachophoresis. Lab Chip 11(22):3793–3801. https://doi.org/10.1039/C1LC20469F
39. Biesiadecki BJ, Tachampa K, Yuan C, Jin JP, de Tombe PP, Solaro RJ (2010) Removal of the cardiac troponin I N-terminal extension improves cardiac function in aged mice. J Biol Chem 285(25): 19688–19698. https://doi.org/10.1074/jbc.M109.086892
40. Akter R, Jeong B, Lee YM, Choi JS, Rahman MA (2017) Femtomolar detection of cardiac troponin I using a novel label-free and reagent-free dendrimer enhanced impedimetric immunosensor. Biosens Bioelectron 91:637–643. https://doi.org/10.1016/j.bios.2017.01.021
41. Han TQ, Yan T, Li YY, Cao W, Pang XH, Huang Q, Wei Q (2015) Eco-friendly synthesis of electrochemiluminescent nitrogen-doped carbon quantum dots from diethylene triamine pentacetate and their application for protein detection. Carbon 91:144–152. https://doi.org/10.1016/j.carbon.2015.04.053
42. Fan DW, Wang HY, Malik SK, Bao CZ, Wang H, Wu D, Wei Q, Du B (2017) An ultrasensitive photoelectrochemical immunosensor for insulin detection based on BiOBr/$Ag_2S$ composite by in-situ growth method with high visible-light activity. Biosens

Bioelectron 97:253–259. https://doi.org/10.1016/j.bios.2017.05.044

43. Yan T, Wu TT, Wei SY, Wang HQ, Sun M, Yan LG, Wei Q, Ju HX (2020) Photoelectrochemical competitive immunosensor for 17β-estradiol detection based on $ZnIn_2S_4$@$NH_2$-MIL-125(Ti) amplified by PDA NS/Mn: ZnCdS. Biosens Bioelectron 148:111739. https://doi.org/10.1016/j.bios.2019.111739
44. Yan PC, Jiang DS, Li HN, Cheng M, Xu L, Qian JC, Bao J, Xia JX, Li HM (2018) Exploitation of a photoelectrochemical sensing platform for catechol quantitative determination using $BiPO_4$ nanocrystals/BiOI heterojunction. Anal Chim Acta 1042:11–19. https://doi.org/10.1016/j.aca.2018.07.063
45. Du MX, Du Y, Feng YB, Li ZF, Wang JY, Jiang N, Liu Y (2019) Advanced photocatalytic performance of novel BiOBr/BiOI/cellulose composites for the removal of organic pollutant. Cellulose 26(9):5543–5557. https://doi.org/10.1007/s10570-019-02474-1
46. Huang HW, Han X, Li XW, Wang SC, Chu PK, Zhang YH (2015) Fabrication of multiple heterojunctions with tunable visible-light-active photocatalytic reactivity in BiOBr-BiOI full-range composites based on microstructure modulation and band structures. ACS Appl Nano Mater 7(1):482–492. https://doi.org/10.1021/am5065409
47. Pang XH, Zhang Y, Pan J, Zhao YH, Chen Y, Ren X, Ma HM, Wei Q, Du B (2016) A photoelectrochemical biosensor for fibroblast-like synoviocyte cell using visible light-activated NCQDs sensitized-ZnO/$CH_3NH_3PbI_3$ heterojunction. Biosens Bioelectron 77:330–338. https://doi.org/10.1016/j.bios.2015.09.047
48. Kang Q, Yang LX, Chen YF, Luo SL, Cai QY, Wen LF, Yao SZ (2010) Photoelectrochemical detection of pentachlorophenol with a multiple hybrid CdSexTe1-x/$TiO_2$ nanotube structure-based label-free immunosensor. Anal Chem 82:9749–9754. https://doi.org/10.1021/ac101798t
49. Ren KW, Wu J, Yan F, Zhang Y, Ju HX (2015) Immunoreaction-triggered DNA assembly for one-step sensitive ratiometric electrochemical biosensing of protein biomarker. Biosens Bioelectron 66:345–349. https://doi.org/10.1016/j.bios.2014.11.046
50. Tuteja SK, Kukkar M, Suri CR, Paul AK, Deep A (2015) One step in-situ synthesis of amine functionalized graphene for immunosensing of cardiac marker cTnI. Biosens Bioelectron 66:129–135. https://doi.org/10.1016/j.bios.2014.10.072
51. Liu DK, Lu X, Yang YW, Zhai YY, Zhang J, Li L (2018) A novel fluorescent aptasensor for the highly sensitive and selective detection of cardiac troponin I based on a graphene oxide platform. Anal Bioanal Chem 410(18):4285–4291. https://doi.org/10.1007/s00216-018-1076-9
52. Chen FF, Wu Q, Song DK, Wang XY, Ma P, Sun Y (2019) $Fe_3O_4$@PDA immune probe-based signal amplification in surface plasmon resonance (SPR) biosensing of human cardiac troponin I. Colloids Surf B Biointerfaces 177:105–111. https://doi.org/10.1016/j.colsurfb.2019.01.053
53. Song SY, Han YD, Kim K, Yang SS, Yoon HC (2011) A fluoro-microbead guiding chip for simple and quantifiable immunoassay of cardiac troponin I (cTnI). Biosens Bioelectron 26(9):3818–3824. https://doi.org/10.1016/j.bios.2011.02.036
54. Luo ZB, Sun DP, Tong YL, Zhong YS, Chen ZG (2019) DNA nanotetrahedron linked dual-aptamer based voltammetric aptasensor for cardiac troponin I using a magnetic metal-organic framework as a label. Mikrochim Acta 186(6):374. https://doi.org/10.1007/s00604-019-3470-1